Copper cobalt tin sulphide (Cu_2CoSnS_4) anodes synthesised using a chemical route for stable and efficient rechargeable lithium-ion batteries

Akbar I. Inamdar,[1, *] Bo Hou,[2, §] Harish S. Chavan[1], Amol S. Salunke[1], Jonghoon Han[1], Giho Shin[1], Sunjung Park[1], Seungun Yeon[1], Nabeen K. Shrestha,[1] Hyunsik Im[1, *] Hyungsang Kim[1, *]

[1]Division of Physics and Semiconductor Science, Dongguk University, Seoul 04620, Republic of Korea

[2] Department of Engineering Science, University of Oxford, Parks Road, OX1 3PJ, UK

[§] Present address: School of Physics and Astronomy, Cardiff University, Cardiff, CF24 3AA, Wales, UK.

In everyday life superior lithium-ion batteries (LIB) with fast charging ability have become a valuable asset. The LIB performance of anode composite copper cobalt tin sulphide (Cu_2CoSnS_4; CCTS) electrodes, which were fabricated using a simple and easy hydrothermal method, was investigated. The electrochemical charge storage performance of the CCTS anode demonstrated sustainability, high-rate capability and efficiency. The CCTS anode exhibited a first discharge capacity of 914.5 $mAhg^{-1}$ and an average specific capacity of 198.7 $mAhg^{-1}$ in consecutive cycles at a current density of 0.1 Ag^{-1}. It had a capacity retention of ~62.0% and a coulombic efficiency of more than 83% after over 100 cycles, demonstrating its excellent cycling performance and reversibility. It can be an alternative anode to other established electrode materials for real battery applications.

***Corresponding Authors**

*E-mail: akbarphysics2002@gmail.com, hyunsik7@dongguk.edu, hskim@dongguk.edu

Introduction

Lithium-ion battery (LIB) is crucial device for storing and transmitting renewable energy produced from wind, solar and tidal.[1] They show a major part in popular daily use electronic devices, electric vehicles, and they also have outstanding properties such as environmental friendliness, high energy density and extended cycle life without memory effect.[2] LIBs are becoming increasingly popular in the automotive market because of their applications in powering electric vehicles and the shortage of fossil energy sources. However, LIBs have a lower energy density than conventional combustion engines. Therefore, the search for energy technologies to balance the demand and supply of energy has become an urgent necessity. The anode in LIBs is crucial because it determines the overall energy and stability of the battery. Although silicon anode has a large theoretical specific capacity, it is ineffective because of its severe volume expansion (more than 300%) during lithiation and delithiation processes.[3] Moreover, graphite is widely studied anode because of its low cost and chemical stability, but its theoretical capacity is extremely low (372 $mAhg^{-1}$), and it has sluggish kinetics.[4] Thus, various materials have been investigated as promising alternative anode materials for LIBs. [5-18].

Tin is known as best anode due to high theoretical capacity of 994 $mAhg^{-1}$, is inexpensive and is non-toxic. For LIBs alloy-type materials and metal chalcogenides are considered outstanding because of high theoretical reversible charge storage capacity.[19] Binary metal chalcogenides, such as MoS_2, WS_2 and ReS_2, have a remarkable potential, but their poor electrical conductivity causes serious issues.[20] Nevertheless, these have stability issue due to structural failure, volume expansion during the charging–discharging process and low conductivity, all of which limit their

practical use. Therefore, it has become important to fabricate alternative anode for LIBs having high energy density and conductivity. Various mechanisms, such as morphology or surface modification, heteroatom doping and encapsulation with carbon-based materials, have been investigated to overcome this problem. Among these mechanisms, heteroatom doping is the most common method for improving the conductivity of materials. Thus, chalcogen materials have attracted significant attention as a dopant for improving the conductivity and stability of LIB alloytype materials. [21,22] Recently, quaternary compounds such as copper zinc tin sulphide (Cu_2ZnSnS_4; CZTS), have attracted significant attention as novel and emerging anode materials for Li-ion batteries [23-26] because they are cost-effective, earth-abundant, environmentally friendly, and structurally/chemically stable.[23] The presence of Sn and Zn, which are electrochemically active, leads to multiple lithiation reactions, while the multi-metal structure offers additional structural flexibility, including a buffer matrix for volume expansion, that allows them to be compositionally engineered to enhance electrochemical performance. Various CZTS morphologies have been fabricated using spray pyrolysis, Rf-magnetron sputtering, electrodeposition, and hot injection. Although structural and electrochemical properties of CZTS are similar to those of copper cobalt tin sulphide (Cu_2CoSnS_4; CCTS), the LIB performance of CCTS anode materials has rarely been investigated. This is an important research task because the synergetic effect between the metal elements in CCTS may generate outstanding properties or functionalities for LIB applications. Therefore, the synergetic effect between various metal atoms may produce novel properties or functionalities in CCTS as a new material for LIB applications.

In this study, we have used easy hydrothermal method to synthesise LIB anode electrodes with a quaternary CCTS compounds. It displays an average specific capacity of 198.7 $mAhg^{-1}$ at

a current density of 0.1 Ag^{-1}. Furthermore, its coulombic efficiency and capacity retention are observed to be 83% and ~62.0%, respectively. Its sustainability after over 100 charge–discharge cycles suggests that it is promising for an anode electrode for real battery applications.

Experimental

Synthesis of CCTS

A CCTS anode was synthesized via hydrothermal technique, followed by slurry coating using a doctor blade technique. Chemicals such as copper chloride, cobalt chloride, tin chloride pentahydrate, thiourea and ethylene glycol were received as raw materials and used without any purification. A precursor solution was prepared in 50 mL of ethylene glycol with a molarities of 0.5 mM copper chloride, 0.25 mM cobalt chloride, 0.25mM tin chloride pentahydrate and 1.25 mM thiourea in. It was mixed properly using a magnetic stirrer for 10 min. The precursor solution was poured into a hydrothermal autoclave jar made by Teflon. The autoclave jar was kept in a furnace at 220°C for 24 h and then left to cool to room temperature. The resulting product was centrifugated at 7000 rpm for 10 min and the collected powder dehydrated in an oven at 60 °C for 24 h. Finally, the powder was ground for 3 h using an agate mortar.

Characterisation

The structural properties were studied using X-ray diffraction (XRD) measurements by Xray diffractometer (PANalytical's X'pert PRO system, Netherlands). It has Cu Kα radiation with a wavelength □ = 1.54056 Å. Raman measurements were carried out at an excitation wavelength of 514 nm using a Labram Aramis spectrometer made by Horiba Jobin. Field emission scanning electron microscopy (model: JSM-6701F, JEOL, made in Japan) was used for surface morphology and compositional analysis. The accelerating voltage during these measurements was of 15 kV.

JEM 2010 transmission electron microscope (JEOL Ltd., made in Japan) and an EDX detector (Oxford Instruments) was used for detailed structural analysis. During these measurements the acceleration voltage was 300 kV and the camera length was 255.8 mm. The chemical oxidation states of the quaternary composite electrode were determined using X-ray photoelectron spectroscopy (model Ulvac-phi, Verse probe II).

LIB fabrication and testing

The coin cell assembly of type CR2032 was used to fabricate LIBs using CCTS as an anode. The Cu foil was used as a current collector for CCTS anode. A slurry was prepared with a composition of CCTS (80%), a binder (10% polyvinylidene fluoride in N-methyl-2-pyrrolidone) and conducting carbon black (10%). The doctor blade technique was used to coat the CCTS slurry uniformly on Cu foil paper. It was subsequently dehydrated overnight at 60 °C for 24 h. A coin cell was made using CCTS disc (15 mm) as an anode and an Li metal disc as a counter electrode in globe box. The globe box was filled with highly pure inert gas such as argon. A 1 M $LiPF_6$ electrolyte with 1:1 volume ratio of ethylene carbonate and dimethyl carbonate was used. The electrochemical properties such charging–discharging in galvanostatic mode, cyclic voltammetry (CV), and alternating current (AC) impedance analyses were carried out using a battery cycler of model MPG-2 made Bio-Logic Science Instruments, in France.

Results and discussion

The structural analysis of the as-prepared CCTS powder is shown in **Figure 1(a)** with standard JCPDS data (no. 26-0513). The strong diffraction peaks at 16.23°, 28.43°, 38.16°, 39.53°, 47.67°, 50.15° and 56.36° of 2θ angles with a reflection along the (002), (112), (211), (114), (204),

(006) and (312) directions, respectively, are assigned to the formation of a phase-pure tetragonal CCTS. It has lattice parameters of a = 5.402 Å and c = 10.80 Å. Our XRD result is reliable with the findings of Wang et al. [27-29]. The other diffraction peaks that do not belong to CCTS are ascribed to secondary phases of SnS (26.6°, 31.3°, 46.6°, and 51.4°, JCPDS-39-0354), CuS (32.1°, JCPDS-79-2321), Cu_2O (36.0°, JCPDS-05-0667), and SnO_2 (54.7°, JCPDS-001-0625). [30, 31]. The Raman technique was used to confirm the purity or to detect the secondary phases in the CCTS structure. **Figure 1(b)** depicts the Raman measurement data of the as-prepared CCTS powder sample. The Raman spectrum has a wide peak in a wavelength between 280–400 cm^{-1}. The deconvolution of the broad peak reveals two peaks at 313.7 and 334.0 cm^{-1}, which are linked to the symmetric vibrations in chalcopyrites such as CCTS. [32]

Morphology and composition analyses of the CCTS powder sample were conducted using SEM and EDX. **Figure 1(c)** and **Figures S1(a)–(b) (**supporting information) depicts the SEM images of as prepared CCTS powder. The images display a large CCTS sheet and overgrown nanograins. **Figure 1(d)** depicts the EDX measurement data of the CCTS powder, evidencing existence of Cu, Co, Sn and S. **Figure S2** depicts the SEM image where the EDX spectra were recorded as well as its original spectra. The atomic ratio between Cu:Co:Sn:S was found to be 2.77:1.0:1.56:3.82

The CCTS sample was also investigated by TEM measurements (**Figures 2(a)–(g)).** A granular structure within a nanometer range can be observed in **Figure 2(a)**. The SAED pattern shown in **Figure 2(b)** depicts clear rings associated with major diffraction peaks of (002), (004), (112) and (110) planes, suggesting that the CCTS structure has high crystallinity (JCPDS-26-0513). Clear lattice fringes are visible in the HRTEM images shown in **Figures 2(c)–(e).** The

lattice distances between the two fringes are found to be 0.32 nm and 0.27 nm, which are associated with the (1 1 2) and (0 0 4) reflections, respectively, of the quaternary CCTS structure. These lattice distances are identical to the standard lattice spacing data provided in JCPDS-26-0513, indicating the formation of the desired composite structure. The HAADF-STEM and EDX mapping images for CCTS in **Figure 2(f)** reveal that Cu, Co, Sn, and S are present in the sample. The STEM elemental line scan profiles in **Figure 2(g)** and the image in **Figure S3** also disclose the same results.

Figures 3(a)–(d) show the deconvoluted XPS spectra of Cu 2p, Co 2p, Sn 3d and S 2p, whereas **Figure S4** shows the survey spectra. The presence of N and O in the survey spectra is possibly due to air contamination. The core-level deconvoluted Cu 2p (**Figure 3(a)**) spectrum displays two peaks at 932.6 eV (Cu $2p_{3/2}$) and 953.1 eV (Cu $2p_{1/2}$). The distance between these two peaks is found to be 20.5 eV, suggesting the existence of Cu^{1+} in the sample. [33] The peaks observed in deconvoluted Co 2p spectrum (**Figure 3(b)**) at 782.08 eV and 794.6 eV, are due to Co $2p_{3/2}$ and its satellite, respectively. It is due to the presence of Co^{2+} oxidation states in the CCTS sample. [34, 35]. The deconvoluted Sn 3d spectrum (**Figure 3(c))** display peaks at 486.05 eV (3d5/2) and 494.6 eV (3d 3/2) are associated with the Sn^{2+} whereas the peaks at 487.03 eV (3d5/2) and 495.3 eV (3d 3/2) are due to Sn^{4+} oxidation states.[36] The S 2p spectrum shown in **Figure 3(d)** showed four peaks, two of which are located at 161.64 eV ($2p_{3/2}$) and 162.9 eV ($2p_{1/2}$), and are due to the sulphide phase. Conversely, the other peaks shown at 169.0 eV are due to the sulphonate formed by the sulphonation reaction with oxygen and air contamination. [37, 38]

The first four CV curves measured at scan rate of 0.1 mVs^{-1} in the potential window of 0.01–3.0 V (vs. Li/Li^{+}) are displayed in **Figure 4(a)**. The observed difference in the CV shape of the first and following cycles is associated with the structural modification, cell polarisation and

solid electrolyte interface (SEI) formation. [5, 6] The first CV curve (**Figure S5**) shows multiple cathodic and anodic peaks (indicated with arrows), which are associated with multistep electrochemical lithium reaction processes and structural rearrangement during the initial surge of Li^{2+} ions. The broad reduction peaks observed at 1.20 V and 0.50 V (vs. Li/Li^+) are due to the irreversible conversion of Li_2S and the reduction of Cu, Co, and Sn, which is caused by the intercalation of Li^+ ions into the CCTS, whereas the peak near 0.2 V is due to the formation of Li_xSn. During the reverse scan, the peaks at 0.54 V, 1.12 V, 1.94 V, and 2.39 V are due to reversible reactions (i.e., the dealloying process) between Sn, Cu, Co, and Li.[39] In subsequent cycles, the cathodic peaks at 1.41 V and 0.79 V (vs. Li/Li^+) are attributed to the intercalation of Li^{2+} or the multistep reduction and conversion of $Li_xCu_2CoSnS_4$ in the metallic phases of Cu, Co, and Sn. [40, 41] The anodic peaks at 0.54 V and 1.12 V (vs. Li/Li^+) are associated with the dealloying of Li_xSn and Li_xCu. The anodic peaks at 0.54 V and 1.12 V (vs. Li/Li^+) are associated with the dealloying of Li_xSn and LixCo. The reaction mechanism during the lithiation process can be described as follows.

$$Cu_2CoSnS_4 + 8\ Li^+ + 8e^- \rightarrow 2\ Cu + Co + Sn + 4Li_2S \quad (1)$$

$$Sn + 4.4\ Li^+ + 4.4\ e^- \rightarrow Li_{4.4}Sn \quad (2)$$

$$Co + 1.5\ Li^+ + 4.4\ e\text{-} \rightarrow Li_{1.5}Co \quad (3)$$

Figure 4(b) depicts the first five galvanostatic charge-discharge (GCD) curves measured at an applied current rate of 0.1 Ag^{-1}. The sloping voltage plateaus seen during discharging and charging are due to the lithiation and delithiation processes, respectively. The first discharge capacity of CCTS is found to be 914.5 $mAhg^{-1}$, which decreased to 198.7 $mAhg^{-1}$. Thus, the capacity loss is expected due to the polarisation and the formation of the SEI layer. This irreversible SEI process showed initial capacity loss in subsequent cycles. In the discharge curve the plateaus seen at 1.41 V and 0.80 V correspond with two cathodic peaks seen in CV, followed by a tail.

When the scan is reversed, two plateaus appear at 0.54 V and 1.12 V, which are ascribed to the reverse course of the conversion reaction. [42] The overlap of GCD curves in the subsequent cycle, indicating excellent cyclic stability. **Figure 4(c)** shows the rate and cycling performances of the CCTS anode at various current densities (0.1 Ag^{-1} and 1.0 Ag^{-1}). The initial discharge capacity is 914.5 $mAhg^{-1}$, it suddenly reduces to 198.7 $mAhg^{-1}$ in consecutive cycles. Thereafter, the charge–discharge capacity becomes stable at each measured current up to 1.0 Ag^{-1}. Interestingly average discharge capacity of 149.7 $mAhg^{-1}$ is obtained when the reversed current density of 0.1 Ag^{-1} is applied. A high-capacity retention of 75.3% is obtained at different current densities.

We conducted ex-situ XPS, XRD, and SEM analyses in fully discharged (to 0.1V) and fully charged (to 3.0 V) states to understand the mechanisms associated with the insertion/extraction of Li^{2+}. Figure 5(a−d) presents the XPS spectra for the CCTS anode in its original, fully discharged, and fully charged states. Cu 2p (Fig. 5a) in the discharged state exhibits three peaks at 932.31, 934.01, and 952.8 eV associated with Cu^{1+}, Cu^{2+}, and metallic Cu^{0} states, respectively.[33] The additional peak at 934.01 eV is presumably due to oxidation of the Cu species in the air. In the charged state, the Cu metallic peak disappears suggesting a reversible reaction to its original Cu^{1+} state. This behaviour is due to the reversible insertion/extraction of Li^{2+} into/from the CCTS anode. The changes in the XPS data during the discharge process can be ascribed to the redox reaction from Cu^{1+} to Cu^{0}. In the Sn *3d* spectra (Fig. 5c), The peaks at 485.9 and 494.6 eV observed in the original sample disappear in the charged and discharged states, suggesting the formation of irreversible Sn^{4+} (487.1 and 495.6 eV) states in the sample [36]. The S *2p* spectra (Fig. 5d) of the original sample show peaks at 161.6 and 162.7 eV, which disappear in the discharged and charged states, and a broad peak at 169.7 appears, which is due to the sulphonate that forms due to the reaction between Li^{2+} and trace amounts of oxygen and water [37,38]. Therefore, it can be concluded that Sn and S are not involved in the reduction reaction. The Co *2p* spectra (Fig. 5b)

also appear to be inactive during the charging−discharging process. To gain more insight into the electrochemical reaction mechanisms within the CCTS anode, exsitu XRD measurements are taken in fully discharged (to 0.01 V) and fully charged (to 3.0 V) states (Fig. S6a). The complete disappearance of the major characteristic diffraction peak at 28.57 ° (112) in CCTS is suggestive of the restructuring of the electrode and the formation of alloys during the first charge−discharge cycle. The XRD patterns in the discharged and changed states are consistent in their structure except for differences in the diffraction intensity, which are due to the reversible partial conversion of the electrode structure during the charge−discharge process. The surface morphology before and after LIB testing is presented in Fig. S6 (b, c). The granular surface of the pristine electrode becomes smooth during the charge−discharge process due to the formation of the SEI layer and Li plating. Thus, the absence of the crakes reveals excellent stability and controlled volume expansion of the CCTS electrode.

Long-term electrochemical stability tests were performed at a current density of $0.1Ag^{-1}$ over 100 cycles. **Figure 6(a)** depicts the specific capacity and coulombic efficiency versus cycle number curves of the CCTS anode electrode for 100 cycles. The coulombic efficiency, discharge and charge capacity after the first cycle are 79.1%, 118.0 $mAhg^{-1}$, and 149.0 $mAhg^{-1}$ respectively. The average coulombic efficiency of the CCTS anode is greater than 83% after over 100 charge–discharge cycles, indicating its excellent stability and reversibility. This coulombic efficiency is better than that of the carbon anode and other anode commercial anodes. [43-45] The specific capacity decreases gradually for the first 50 cycles before stabilising after over 100 charge–discharge cycles. The CCTS anode electrode had ~62.0% and ~56.2%, discharge and charge capacity retentions, with a capacity loss of 0.38% and 0.43% per cycle.

Quantitative estimation is carried out via CV measurements at different scan rates to determine the capacitive and diffusion-limited contributions to the total capacity of the electrode. **Fig. 6(b)** presents the CV curves measured at different scan rates of 0.2, 0.5, 1.0, 2.0, and 5.0 mVs^{-1}. The cathodic and anodic currents obey the power law relationship with the scan rate. Thus, the Li-ion intercalation kinetics can be estimated using the following power law [6, 45]

$$i = a \times \nu^{b} \qquad (1)$$

where a and b are the fitting parameters, and ν is the scan rate. The slope of the plot $\log(i)-\log(\nu)$ gives information about the diffusion−controlled and capacitive-type storage mechanisms. **Figure S7** presents the $\log(i)-\log(\nu)$ plots, with the slopes for the cathodic and anodic currents estimated to be 1.24 for peak C1, 0.53 for peak C2, and 0.54 for peak A1. This indicates that the reaction current is due to the contribution of intercalation and capacitive-type storage mechanisms. The quantitative capacitive contribution from the total current is obtained using Eq. (2):

$$i = k_1 \times \nu + \kappa_2 \times \nu^{1/2} \qquad (2)$$

where k_1 and k_2 are the fitting parameters, and i is the current at a fixed potential. $k_1 \times \nu$ is the capacitive contribution, and $k_2 \times \nu^{1/2}$ represents the diffusion-controlled contribution. k_1 and k_2 can be estimated from the $\nu^{1/2}$ vs. $i/\nu^{1/2}$ plot using the slope of the curve and the y-axis intercept, respectively (**Figure S8**). The relative contributions of the capacitive and diffusion-controlled storage mechanisms are presented in **Fig. 6(c)**. Although the capacitive contribution decreases with the scan rate, it is more than 85% even at high scan rates, indicating that the major contribution comes from capacitive-type mechanisms.

Electrochemical impedance spectroscopy (EIS) was conducted to determine the electrochemical resistance of the CCTS anode and electrolyte interface. **Figure 6(d)** presents Nyquist plots recorded after 100 GCD cycles for different applied voltages. The inset of the figure

presents the equivalent circuit diagram, with *Rs* indicating the solution resistance. The Nyquist plots show semicircles and a straight line, which represent the charge transfer resistance (R_{ct}) and Warburg impedance (*Wo*), respectively. The increase in the semi-circle diameter with an increase in the potential from the open circuit potential (OCP) to 2.0 V indicates that the charge-transfer resistance increases. [45, 46] This resistance is 107.0 Ω at the OCP (0.0 V), while it is 117.5 Ω and 136.0 Ω at 1.0 V and 2.0 V, respectively. The slope of the straight-line decreases in the low frequency region as the potential increases, indicating poor capacitive behaviour at high voltages. The obtained parameters are presented in Table S1. This indicated that the electrode resistance decreased during discharge process. Moreover, the decreased slope of the straight line in the low frequency region with respect to potential indicated the bad capacitive behaviours at high voltages.

Conclusions

We fabricated CCTS anode electrodes for LIBs using a simple hydrothermal technique. The formation of nearly stoichiometric CCTS with a composition ratio of $Cu_{2.77}Co_{1.0}Sn_{1.56}S_{3.82}$ is observed. The shape of the GCD curves remains unchanged during consecutive cycles, representing that the CCTS anode electrode had a stable charge storage mechanism. The CCTS anode electrode has a reversible average discharge capacity of 198.7 $mAhg^{-1}$ at a current density of 0.1 Ag^{-1}. It has excellent capacity retention of 62.0% and a coulombic efficiency of more than 83% after over 100 charge–discharge cycles. A capacity retention of 75.3% is found after charge–discharge cycles at various current densities, indicating high-rate performance. Overall, the electrochemical charge storage performance of the CCTS anode is sustainable and efficient.

Acknowledgments

This work was supported by the Basic Science Research Program of the National Research Foundation of Korea (2018R1D1A1B07049046, 2021R1A2B5B01001796 and 2021R1A4A5031805).

Conflicts of interest

There are no conflicts to declare.

Author contributions

A.I.I., N.K.S., H.K., and H. I. designed the experiments and wrote the manuscript. H.S.C., A.S S. carried out the experiments and extracted data for the analysis. J.H., G.S., S.P., S.Y. helped for data analysis. B.H. carried out electron microscopy. All of the authors have reviewed and approved the final version of the manuscript.

Notes and References

[1]. M. C. Han, L. L. Zhu, Y. M. Li, F. Wei, Y. Shi, *Dalton Trans.,* 2021, **50**, 11137.

[2]. T. F. Yi, H. M. K. Sari, X. Z. Li, F. F. Wang, Y. R. Zhu, J. H. Hu, J. J. Zhang and X. F. Li, *Nano Energy*, 2021, **85**, 105955.

[3]. L. Zhang, R. Rajagopalan, H. Guo, X. Hu, S. Dou, H. Liu, *Adv. Funct. Mater.,* 2016, **26**, 440.

[4] X. Liu, T. Najam, G. Yasin, M. Kumar, M. Wang, *ACS Omega,* 2021, **6**, 17391.

[5] A. I. Inamdar, R. S. Kalubarme, J. Kim, Y. Jo, H. Woo, S. Cho, S. M. Pawar, C. J. Park, Y. W. Lee, J. I. Sohn, S. Cha, J. Kwak, H. Kim, H. Im, *J. Mater. Chem. A,* 2016, **4,** 4691.

[6] A. I. Inamdar, A. T. A. Ahmed, H. S. Chavan, Y. Jo, S. Cho, J. Kim, S. M. Pawar, B. Hou, S. Cha, H. Kim, H. Im, *Ceram. Int.* 2018, **44**, 18625.

[7] S.M. Pawar, B.S. Pawar, Bo Hou, A.T.A. Ahmed, H.S. Chavan, Yongcheol Jo, Sangeun Cho, Jongmin Kim, Jiwoo Seo, SeungNam Cha, A.I. Inamdar, Hyungsang Kim, Hyunsik Im, *J. Indus. Eng. Chem.* 2019, **69**, 13.

[8] A. I. Inamdar, H. S. Chavan, A. T. A. Ahmed, Y. Jo, S. Cho, J. Kim, S. M. Pawar, H. Kim, H. Im, *J. Alloys and Compds.* 2020, **829,** 154593.

[9] J. Kim, Y. Jo, A. T. A. Ahmed, A. I. Inamdar, S. Cho, H. Kim, H. Im, *Int J Energy Res.* 2022, **46**, 1387.

[10] S. Nagarajan, S. Hwang, M. Balasubramanian, N. K. Thangavel, L. M. Reddy Arava, *J. Am. Chem. Soc.* 2021, **143**, 15732.

[11] C. J. Hansen, J. J. Zak, A. J. Martinolich, J. S. Ko, N. H. Bashian, F. Kaboudvand, A. Van der Ven, B. C. Melot, J. Nelson Weker, K. A. See, *J. Am. Chem. Soc.* 2020, **142,** 6737.

[12] T. Wang, G. X. Ren, Z. Shadike, J. L. Yue, M. H. Cao, J. N. Zhang, M. W. Chen, X. Q. Yang, S. M. Bak, P. Northrup, P. Liu, X. S. Liu, Z. W. Fu, *Nat. Commun.* 2019, **10**, 4458.

[13] S. Saha, G. Assat, M. T. Sougrati, D. Foix, H. Li, J. Vergnet, S. Turi, Y. Ha, W. Yang, J. Cabana, G. Rousse, A. M. Abakumov, J. M. Tarascon, *Nature Energy,* 2019, **4**, 977.

[14] X. Wang, Q. Wei, H. Li, J. Sun, H. Li, Y. He, Z. Liu, *J. Mater. Chem. A,* 2022, **10**, 7517.

[15] Q. Zheng, Y. Yamada, R. Shang, S. Ko, Y. Y. Lee, K. Kim, E. Nakamura, A. Yamada, *Nature Energy,* 2020, **5,** 291.

[16] H. Wu, X. Zou, X. L. Wu, *Nano Futures,* 2020, **4**, 042001.

[17] T.V.S.L. Satyavani, A. Srinivas Kumar, P.S.V. Subba Rao, *Eng. Sci. Technol. an Int. J.,* 2016, **19**, 178.

[18] A. Marongiu, F. G. W. Nußbaum, W. Waag, M. Garmendia, D. U. Sauer, "*Appl. Energy*, 2016, **171,** 629.

[19] J. Cabana, L. Monconduit, D. Larcher, M. Rosa Palacín, *Adv. Mater.,* 2010, **22,** E170.

[20] C. (John) Zhang, S. H. Park, O. Ronan, A. Harvey, A. S. Ascaso, Z. Lin, N. McEvoy, C. S. Boland, N. C. Berner, G. S. Duesberg, P. Rozier, J. N. Coleman, V. Nicolosi, *Small,* 2017, **13**, 1701677.

[21] X. Zhou, L. Liu, S. Zhu, J. Niu, X. Cai, J. Zheng, Y. Ye, L. Lin, Z. Zheng, D. Zhu, Z. Sun, Y. Lu, Y. Zang, J. Wu, Q. Xiao, Y. Liu, G. Zhu, Y. Wang, Y. Qian, *Chem.,* 2020, **6 (1),** 221.

[22] J. Q. Zhou, T. Qian, N. Xu, M.F. Wang, X.Y. Ni, X.J. Liu, X.W. Shen, C.L. Yan, Adv. *Mater.,* 2017, **29 (33),** 1701294.

[23] Q. Jiang, X. Chen, H. Gao, C. Feng, Z. Guo, *Electrochim. Acta* 2016, **190**, 703.

[24] J. Lin, J. Guo, C. Liu, H. Guo, *ACS Appl. Mater. Interfaces* 2015, **7**, 17311.

[25] X. Yin, C. Tang, M. Chen, S. Adams, H. Wang, H. Gong, *J. Mater. Chem. A* 2013, **1**, 7927.

[26] Z. Syum, T. Billo, A. Sabbah, B. Venugopal, S. Y. Yu, F. Y. Fu, H. L. Wu, L. C. Chen, K. H. Chen, *ACS Sustainable Chem. Eng.* 2021, **9**, 8970.

[27] J. Zhong, Q. Wang, W. Cai, *Mater. Letters,* 2015, **150,** 69.

[28]. M. Beraicha, M. Taibi, A. Guenbour, A. Zarrouk, M. Boudalia, A. Bellaouchou, M. Tabyaoui, S. Mansouri, Z. Sekkat, M. Fahoum, *Optik,* 2019, **193**, 162996.

[29]. I. Bargaoui, N Bitri, S Dridi, I. Ly, *Mater. Res. Express,* 2019, **6,** 086410.

[30]. D. Li, J. Ma, L. Zhou, Y. Li, C. Zou, *Optik,* 2015, **126,** 4971.

[31] D. Ma, W. Zhang, Q. Tang, R. Zhang, W. Yu, Y. Qian, *J. Nanosci. Nanotechnol.,* 2005, **5(5),** 806.

[32] A. Gillorin, A. Balocchi, X. Marie, P. Dufoura, J. Y. Chane-Ching, *J. Mater. Chem.,* 2011, **21**, 5615.

[33]. T. Wang, Q. Zhan, W. Cheng, *J. Mater. Sci.:Mater. Electron.,* 2019, **30**, 2285.

[34] Y. Hou, H. Pang, J. Xin, H. Ma, B. Li, X. Wang, L. Tan, *Adv. Mater. Interfaces,* 2020, **7**, 2000780.

[35] S. He, H. Du, K. Wang, Q. Liu, J. Sun, Y. Liu, Z. Du, L. Xie, W. Ai, W. Huang, *Chem. Commun.,* 2020, **56,** 5548.

[36] F. F. H. Aragon, J. C. R. Aquino, L. Villegas-Lelovsky, M.C. Mathpal, L. Cabral, M. P. Lima, J. A. H. Coaquira, S. W. da Silva, L. C. C. M. Nagamine, S. O. Parreiras, P. L. Gastelois, G. E. Marques, W. A. A. Macedo, *Phys. Chem. Chem. Phys.,* 2020, **22**, 3702.

[37] Y. Wu, T. Momma, S. Ahn, T. Yokoshima, H. Nara, T. Osaka, *J. Power Sources,* 2017, **366,** 65.

[38] H. Chu, H. Noh, Y. J. Kim, S. Yuk, J. H. Lee, J. Lee, H. Kwack, Y. K. Kim, D. K. Yang, H. T. Kim, *Nature Commn.,* 2019, **10**, 188.

[39] Y. Li, Z. Liu, X. Cheng, X. Liu, B. Zhang, D. Sun, R. Wang, Y. Zhang, *Energy Storage Mater.,* 2017, **9,** 188.

[40] H. Chen, J. He, G. Ke, L. Sun, J. Chen, Y. Li, X. Ren, L. Deng, P. Zhang, *Nanoscale*, 2019, **11**, 16253.

[41] B. Sun, Q. Zhang, C. Zhang, W. Xu, J. Wang, G. Yuan, W. Lv, X. Li, N. Yang, *Adv. Energy Mater.* 2021, **11**, 2100082.

[42] Z. Cao, B. Wei, *Front. Mater.,* 2015, **2**, article 40.

[43] B. Guo, J. Shu, K. Tang, Y. Bai, Z. Wang, L. Chen, *J. Power Sources,* 2008, **177,** 205.

[44] Y. Sun, L. Zhao, H. Pan, X. Lu, L. Gu, Y. S. Hu, H. Li, M. Armand, Y. Ikuhara, L. Chen, X. Huang, *Nat. Commun,* 2013, **4**, 1870.

[45] A. Rudola, K. Saravanan, C. W. Mason, P. Balaya, *J. Mater. Chem. A,* 2013, **1**, 5653.

[46] S. Lou, X. Cheng, Y. Zhao, A. Lushington, J. Gao, Q. Li, P Zuo, B. Wang, Y. Gao, Y. Ma, C. Du, G. Yin, X. Sun, *Nano Energy* 2017, **34**, 15.

[47] J. Im, J. Lee, M. H. Ryou, Y. M. Lee, K. Y. Cho. *J. Electrochem. Soc.*2017, **164**, A6381. [48] F. Ebadi, N. Taghavinia, R. Mohammadpour, A. Hagfeldt, W. Tress. *Nature Commun*., 2019, **10,** 1574.

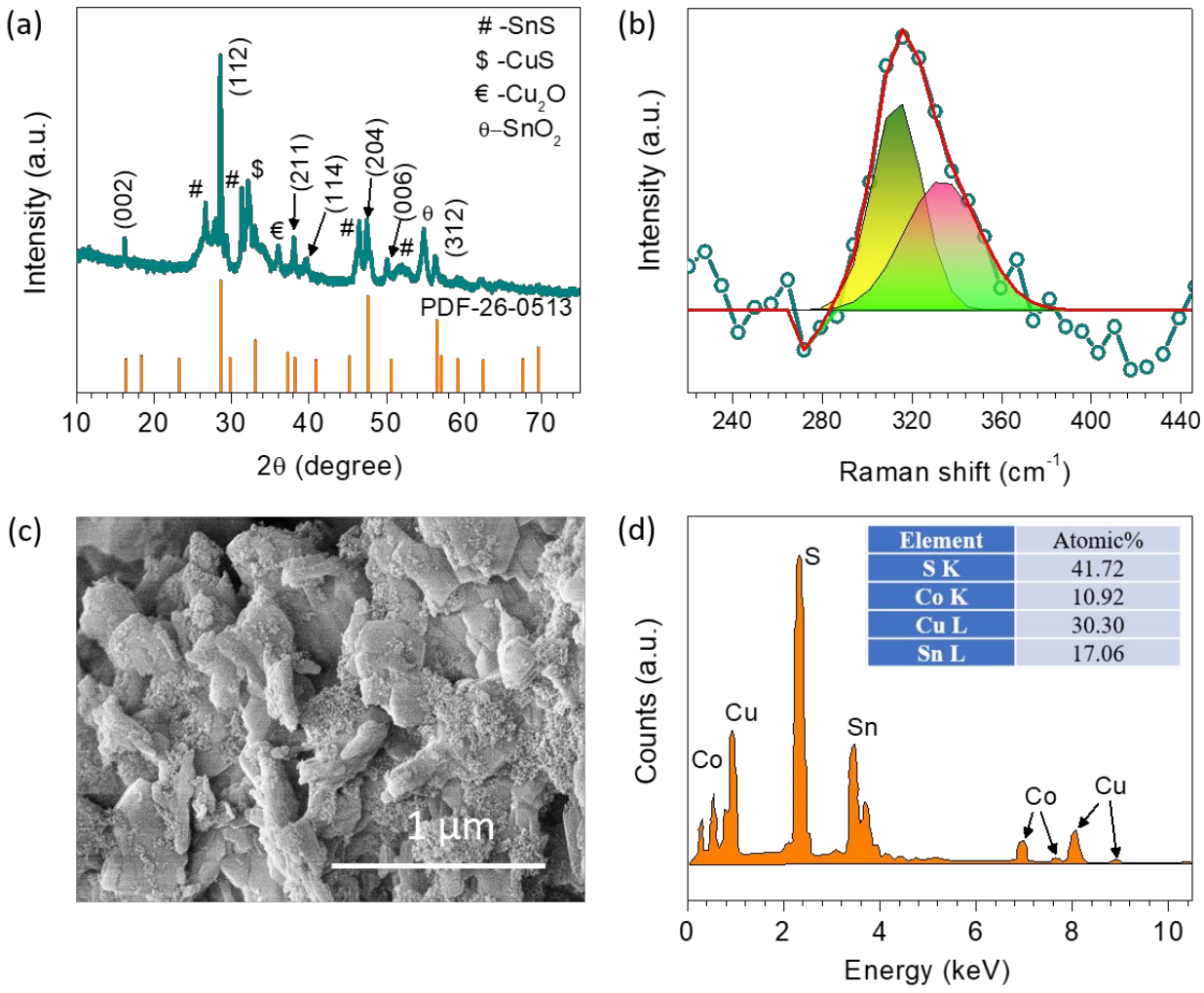

Figure 1. (a) X-ray-diffraction (XRD) pattern of the CCTS powder and the JCPDS 26-0513 data. (b) Raman spectra recorded at an excitation wavelength of 514 nm in a wavelength range of 280400 cm^{-1}. The circles and lines represent the experimental data and fitted curves, respectively. (c) SEM image and (d) energy dispersive X-ray (EDX) analysis spectrum of CCTS. The inset table shows the actual atomic percentage of the constituent elements.

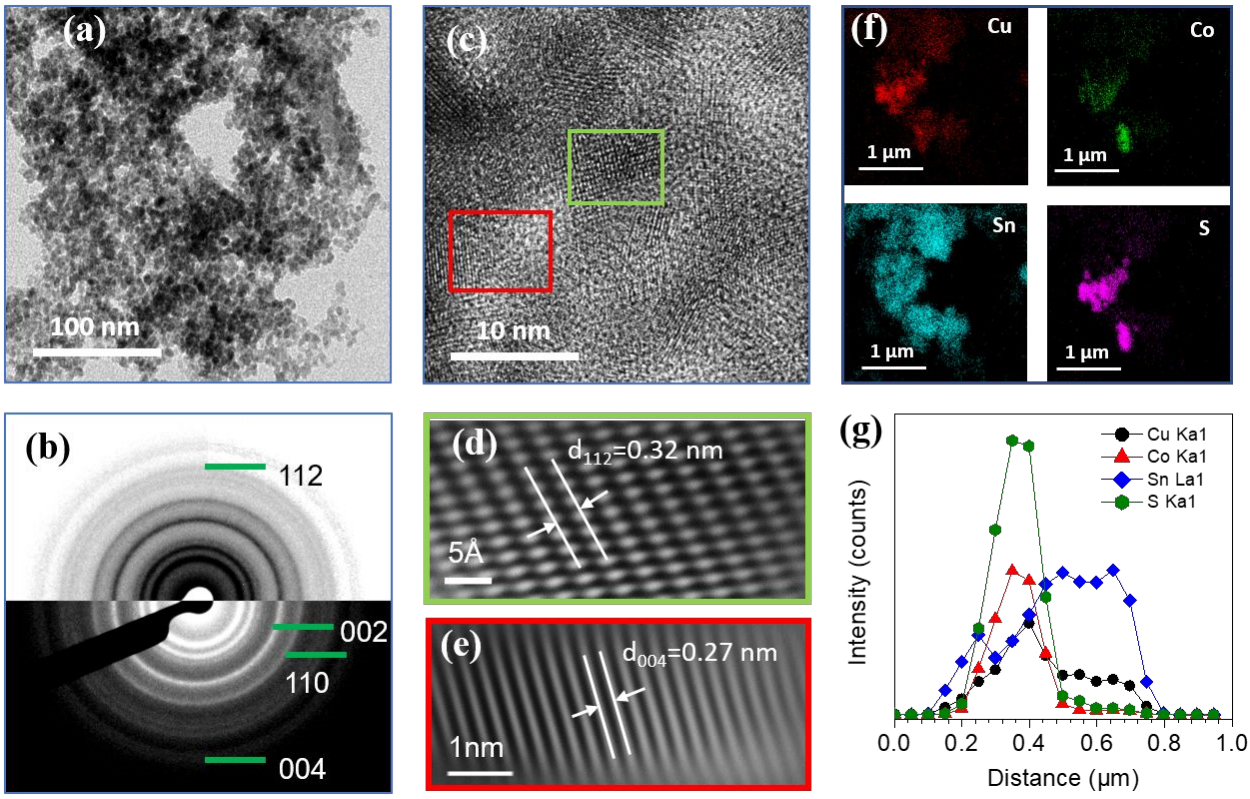

Figure 2. (a) Transmission-electron-microscopy (TEM) image, (b) selected-area-electrondiffraction (SAED) pattern, (c) high-resolution transmission-electron-microscopy (HRTEM) image, (d) and (e) clear lattice fringes observed in the selected area of the HRTEM image. The lattice distances for the selected areas, d_{112} and d_{004} are 0.32nm and 0.27 nm respectively. (f) Highangle annular dark field-scanning transmission electron microscopy (HAADF-STEM) elemental mapping under TEM mode revealing the homogeneous distribution of Cu (red), Co (green), Sn (cyan) and S (pink) in the sample. (g) STEM elemental line scan profiles of the CCTS anode electrode.

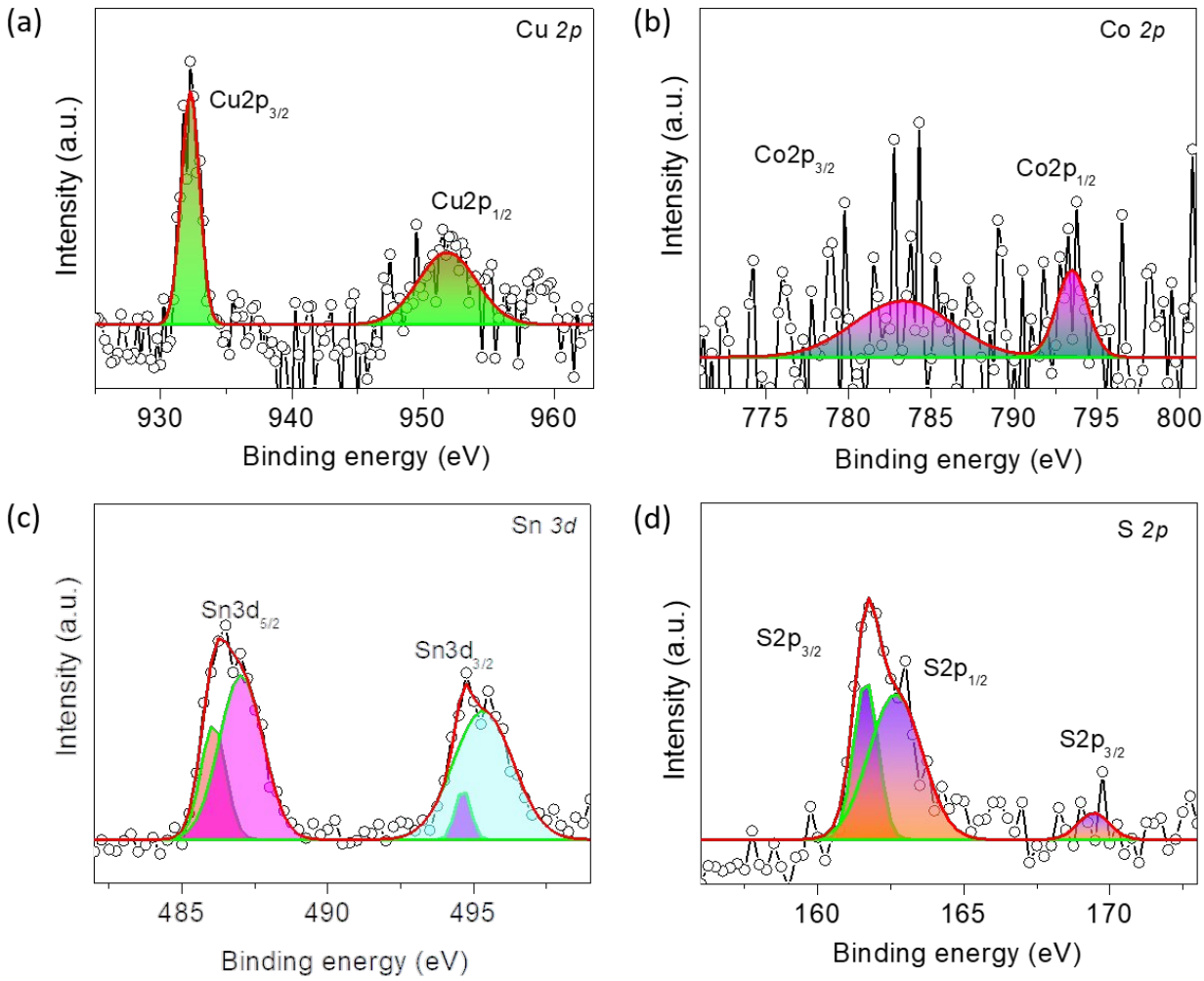

Figure 3. X-ray photoelectron spectroscopy (XPS) spectra of the CCTS anode electrode. (a) deconvoluted Cu 2p peaks, (b) deconvoluted Co 2p peaks, (c) deconvoluted Sn 3d peaks, and (d) deconvoluted S 2p peaks. The circles and lines represent the experimental data and fitted curves, respectively.

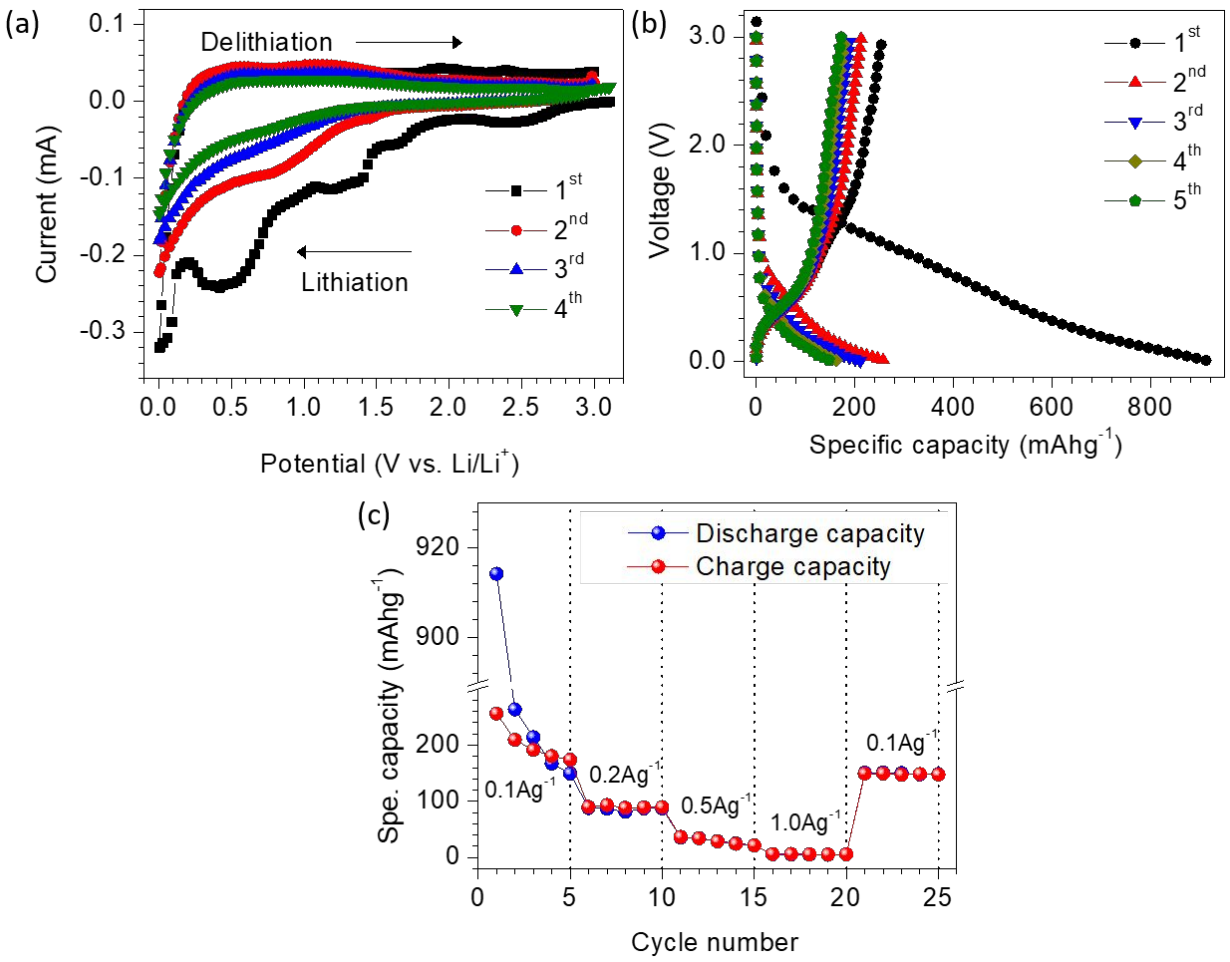

Figure 4. (a) Initial four cycles of the cyclic-voltammetry (CV) curves of the CCTS electrode measured at a scan rate of 0.1 mVs^{-1}. (b) Galvanostatic charge-discharge characteristics of the CCTS electrode recorded at a current of 0.1 Ag^{-1} for the first five cycles. (c) rate performances of the CCTS electrode at different currents.

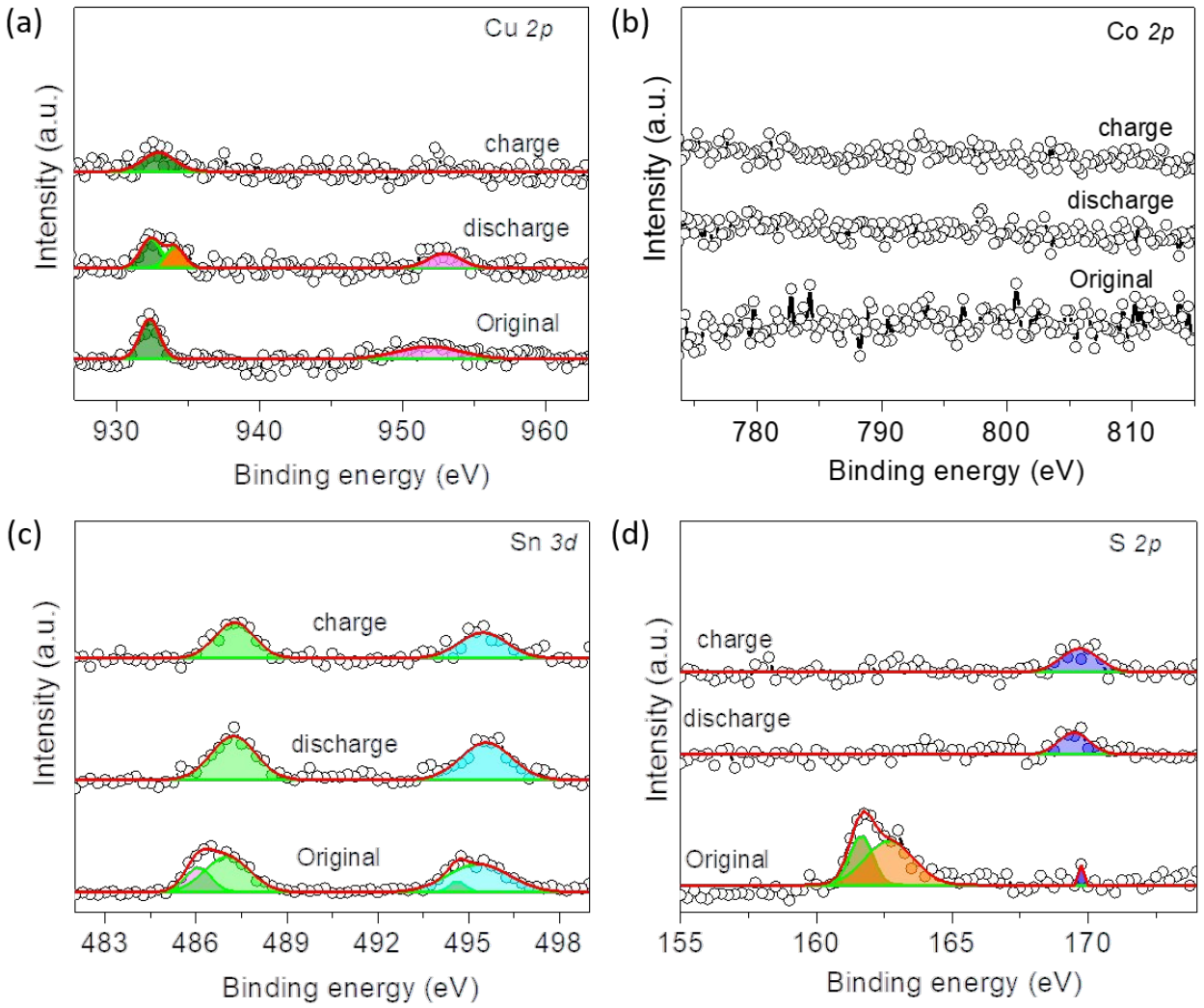

Figure 5. Ex-situ XPS analysis of the CCTS anode after fully discharged to 0.1 V and fully charged to 3.0 V, (a) deconvoluted Cu 2p peaks, (b) deconvoluted Co 2p peaks, (c) deconvoluted Sn 3d peaks, and (d) deconvoluted S 2p peaks. The circles and lines represent the experimental data and fitted curves, respectively.

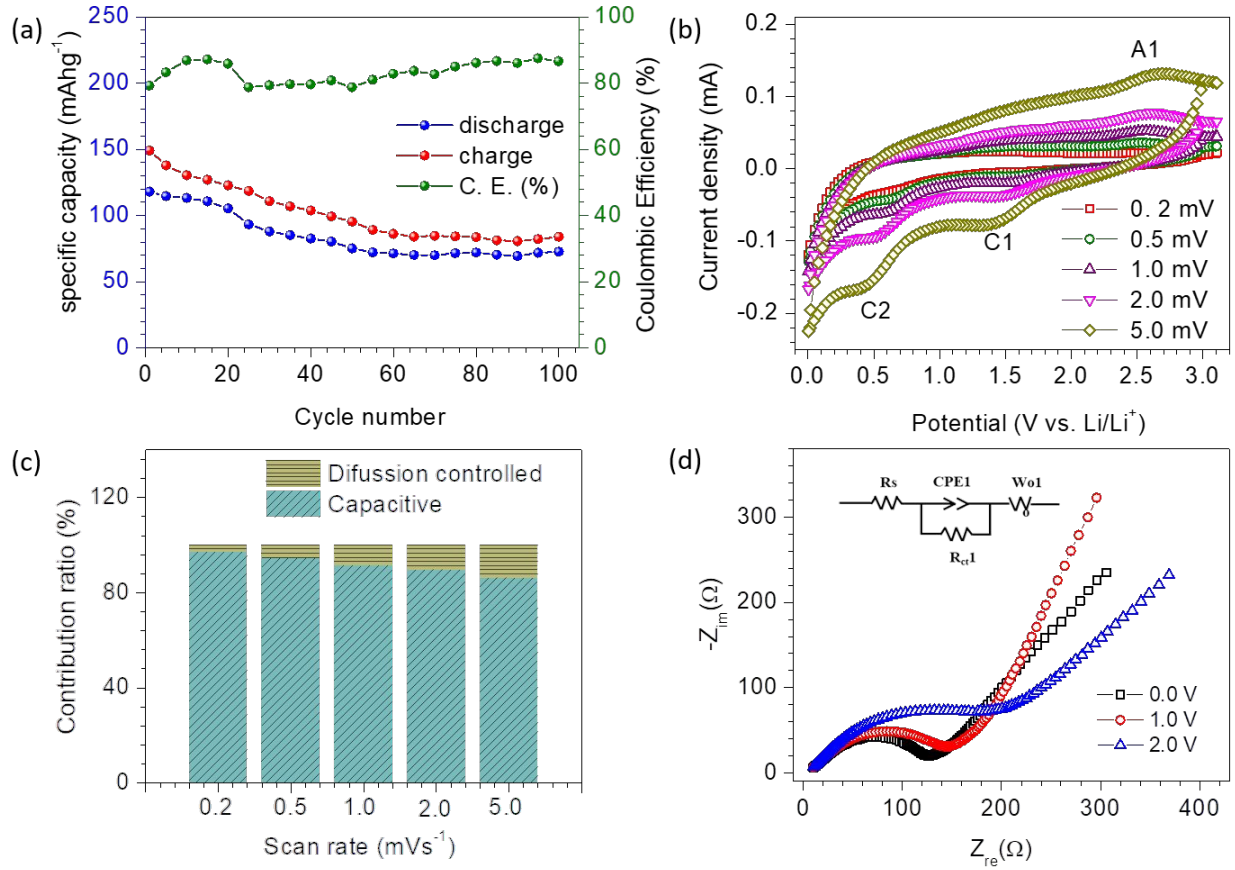

Figure 6. (a) Long-life-cycling performance and coulombic efficiency of the CCTS anode at 0.1 Ag^{-1} (b) Cyclic-voltammetry (CV) curves at scan rates of 0.2, 0.5, 1.0, 2.0, and 5.0 mVs^{-1}, (c) Comparison of the capacitive and the diffusion-controlled charge storage at different scan rates, and (d) Nyquist plots at different voltages (inset shows equivalent circuit diagram).

Table of contents

We demonstrate lithium-ion batteries (LIBs) performance of a novel Cu_2CoSnS_4 (CCTS) electrode as an anode prepared by hydrothermal method. It exhibits specific capacity of 198.7 $mAhg^{-1}$, 83% coulombic efficiency, excellent rate capability and capacity retention.

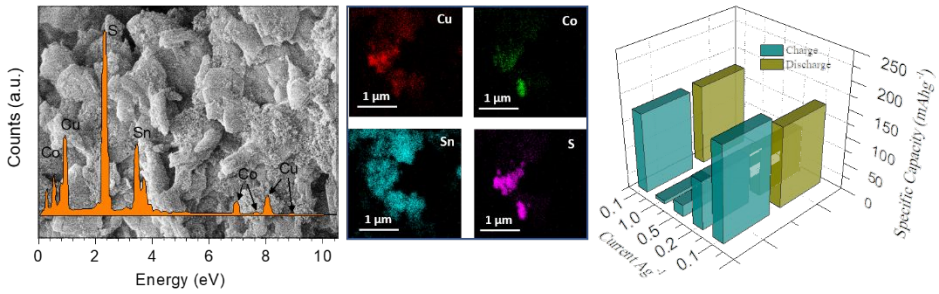

Supporting Information

Copper cobalt tin sulphide (Cu_2CoSnS_4) anodes synthesised using a chemical route for stable and efficient rechargeable lithium-ion batteries

Akbar I. Inamdar,[1, Z] Bo Hou,[2, =] Harish S. Chavan[1], Amol S. Salunke[1], Jonghoon Han[1], Giho Shin[1], Sunjung Park[1], Seungun Yeon[1], Nabeen K. Shrestha,[1] Hyunsik Im[1, Z] Hyungsang Kim[1, Z]

[1]Division of Physics and Semiconductor Science, Dongguk University, Seoul 04620, Republic of Korea

[2] Department of Engineering Science, University of Oxford, Parks Road, OX1 3PJ, UK

[=] Present address: School of Physics and Astronomy, Cardiff University, Cardiff, CF24 3AA, Wales, UK.

*E-mail: akbarphysics2002@gmail.com, hyunsik7@dongguk.edu, hskim@dongguk.edu

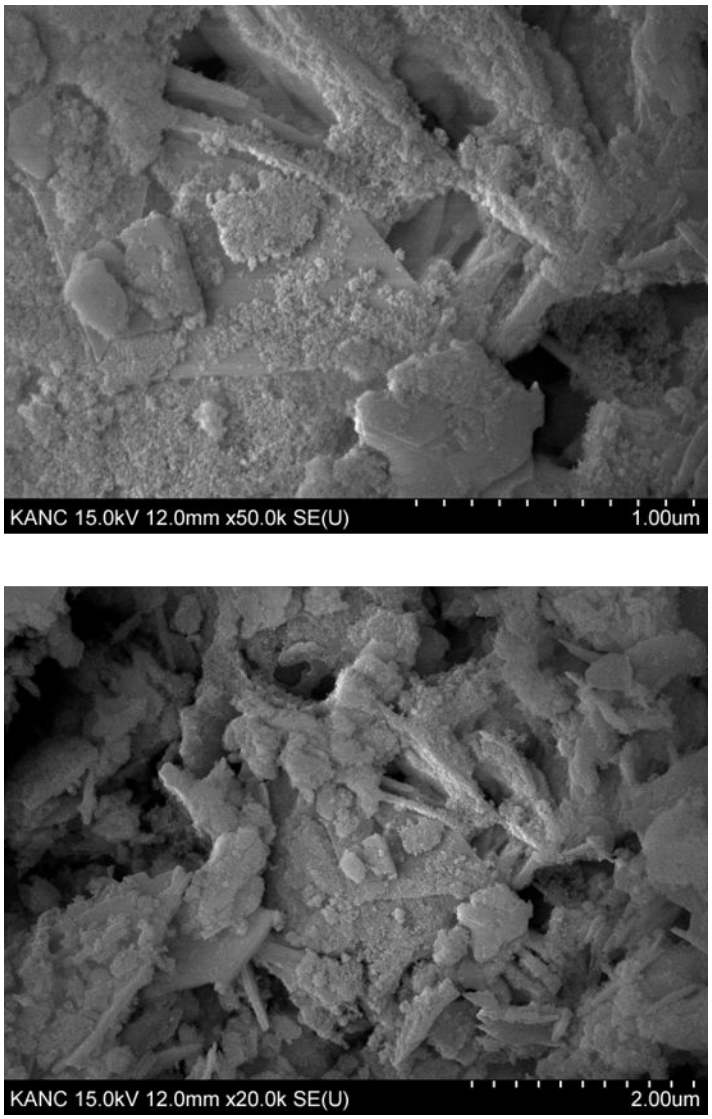

Figure S1. Scanning electron microscope (SEM) images of the CCTS powder sample exhibit large-sized CCTS sheets and overgrown nanograins.

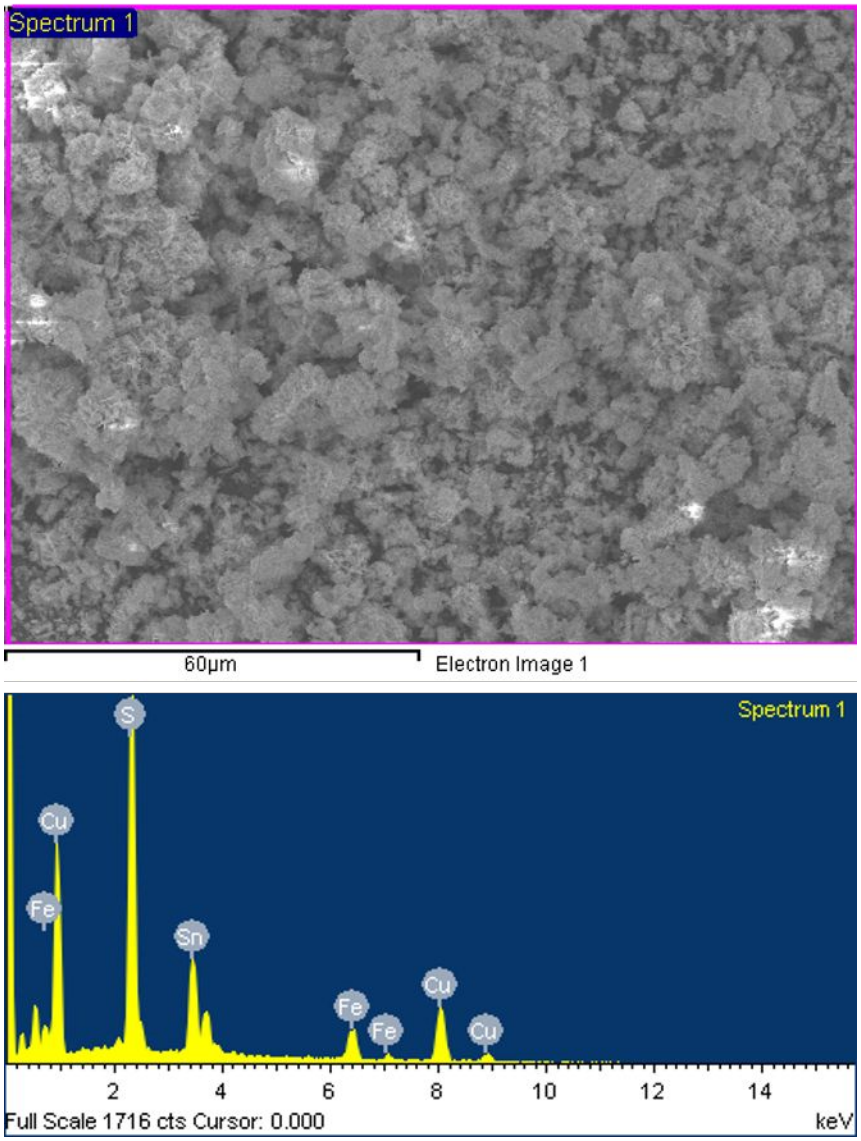

Figure S2. Low magnified SEM image of the CCTS powder electrode and the point where EDS spectrum recorded.

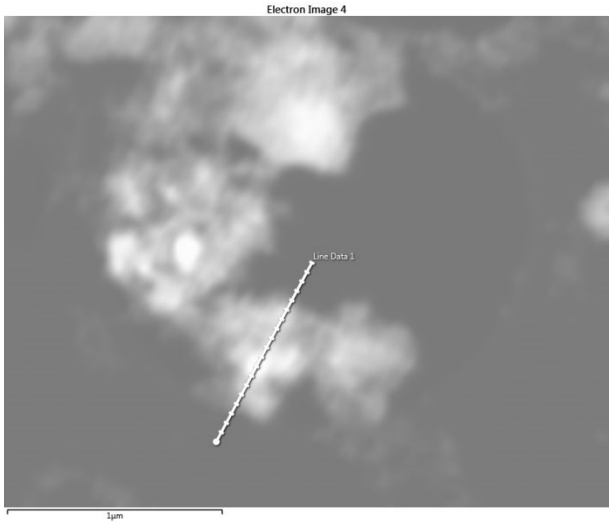

Figure S3. High-angle annular dark-field-scanning transmission electron microscopy (HAADFSTEM) image where the STEM elemental line scan profile was recorded (Figure 2(g) in the main text).

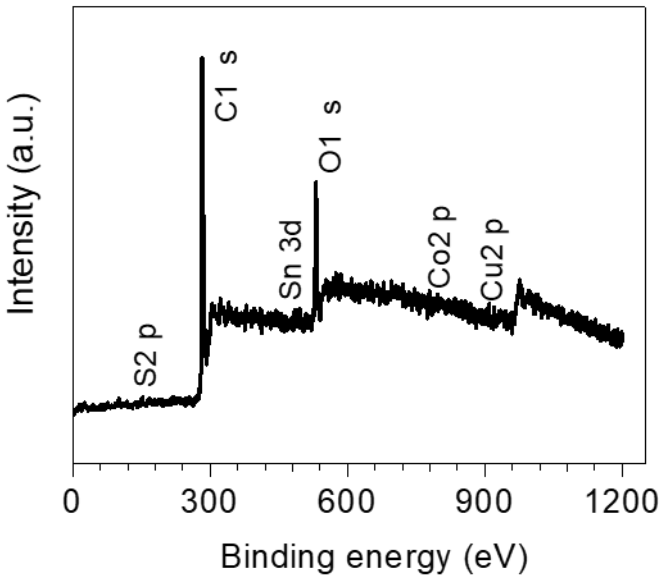

Figure S4. X-ray photoelectron spectroscopy (XPS) survey spectrum of the CCTS powder electrode revealing the presence of the main elements Cu, Co, Sn and S.

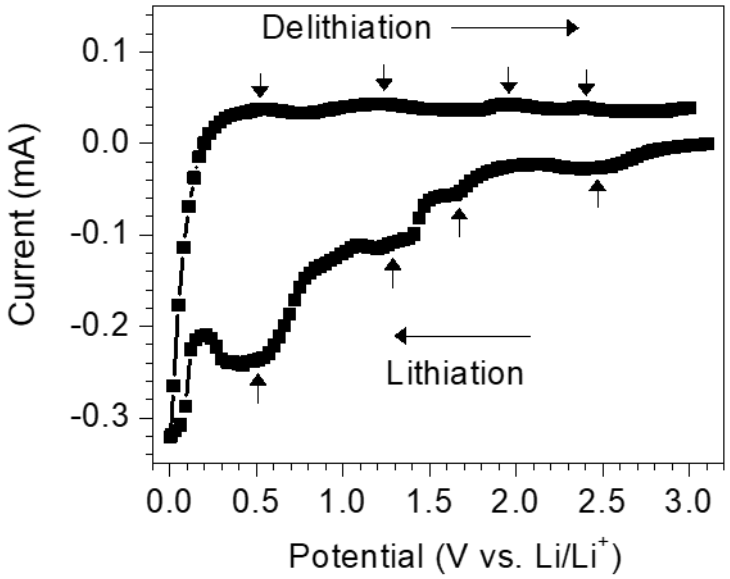

Figure S5. The first CV curve of the CCTS anode electrode recorded in the potential window between 0.01 and 3.0 V (vs. Li/Li^+) at a scan rate of 0.1 mVs^{-1}. The multiple cathodic and anodic peaks marked with arrows are associated with the phase transition and structural rearrangement during the initial surge of the Li^{2+} ions.

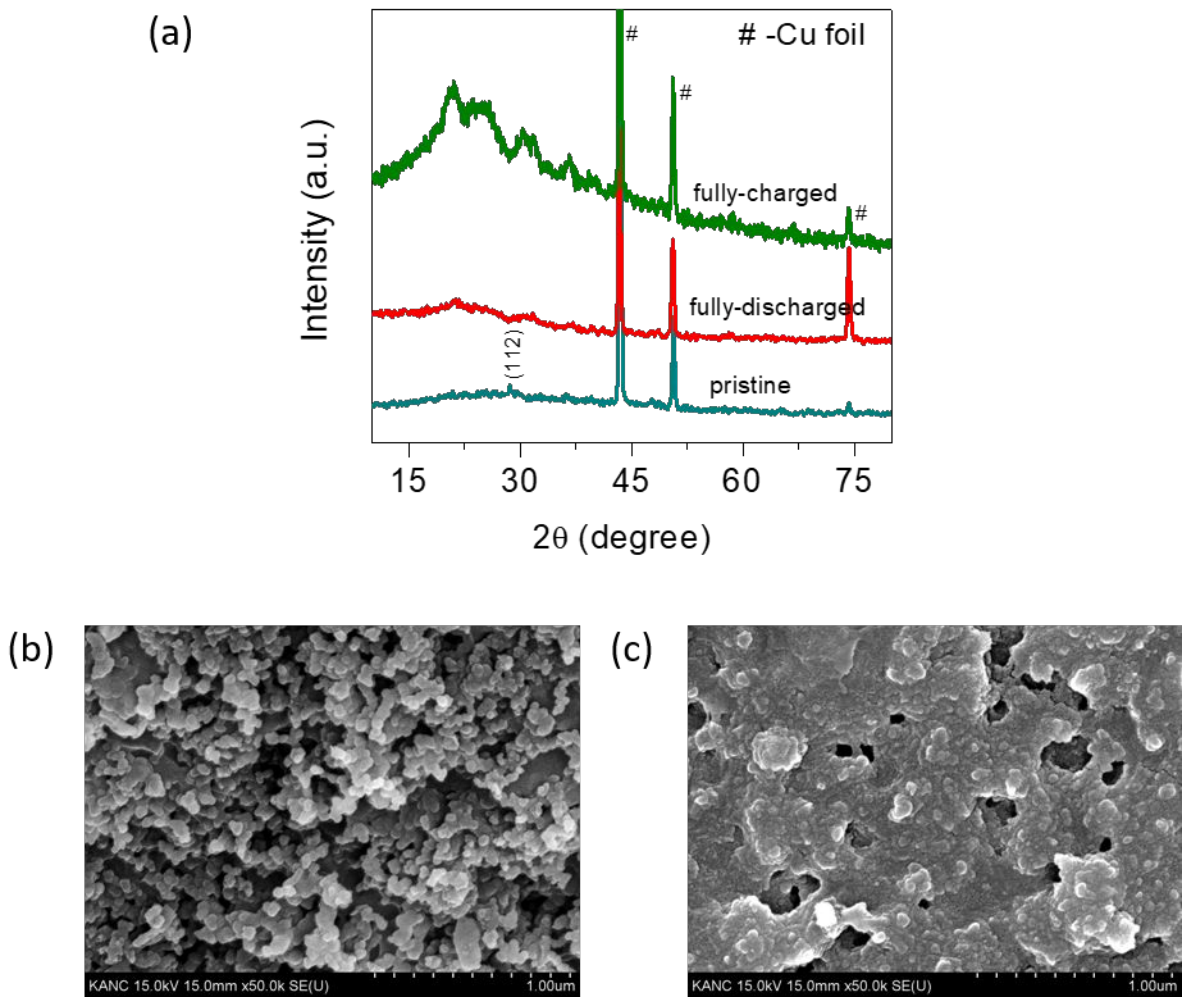

Figure S6. (a) Ex-situ X-ray diffraction spectra of CCTS in the fully charged to 3.0 V and fully discharged to 0.01 V states. Ex-situ SEM morphologies of the CCTS anode electrode (b) as grown CCTS electrode onto Cu-foil paper, (c) after Li-ion battery test.

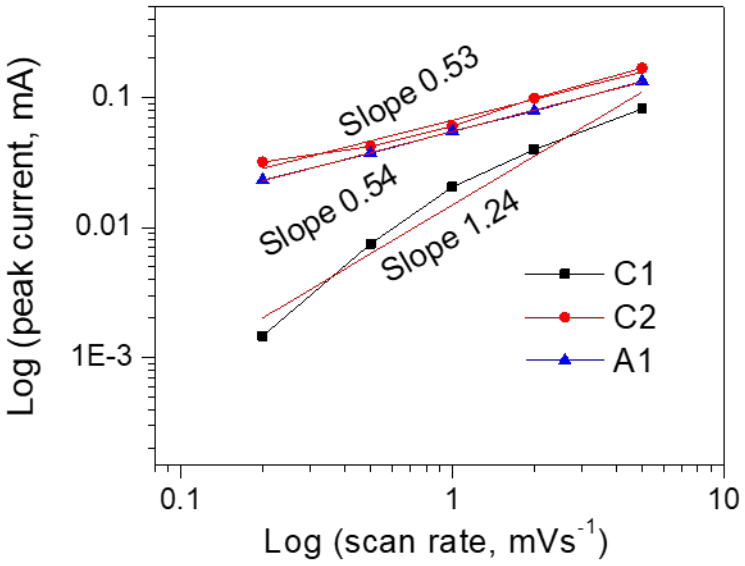

Figure S7. The slope of log (i) vs log (ν) curves giving information on the mechanism exhibited by into the electrode. If the slope is less than 0.5 it is diffusion controlled and if the slope is more than 1 it is controlled by the capacitive-type storage mechanism.

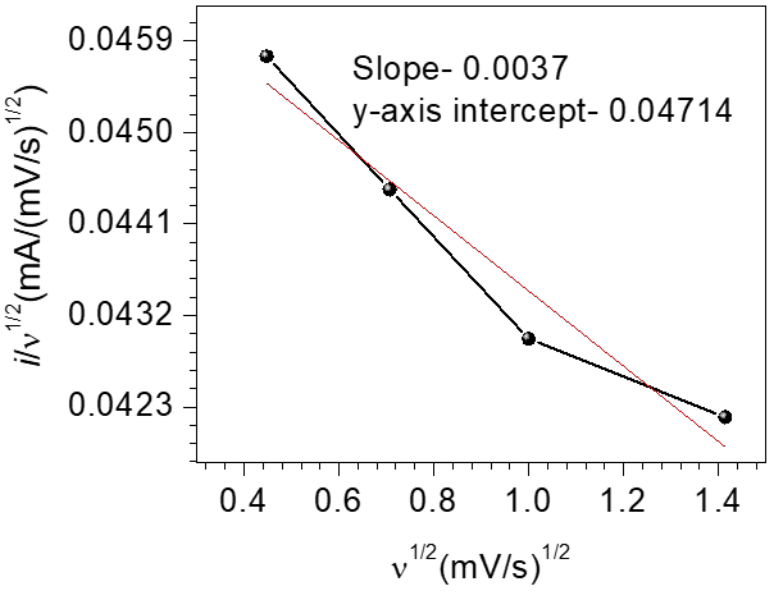

Figure S8. The capacitive contribution and diffusion-controlled contribution are calculated using by plotting $v^{1/2}$ versus $i/ v^{1/2}$.

Table S1- Parameters obtained by fitting of Nyquist plot using Zfit software as a function of potential.

Sr. No.	Potential (V)	Solution resistance *Rs* (Ω)	Charge-transfer resistance *Rct* (Ω)	Warburg impedance *W* (Ω.s$^{-1/2}$)
1.	0.0	8.7	107	114.5
2.	1.0	9.2	117.5	218
3.	2.0	9	136	650